EUROPEAN FUSION DEVELOPMENT AGREEMENT
JET

EFDA–JET–CP(04)01/09

R Barnsley, M.O'Mullane, L.C. Ingesson, A. Malaquias
and JET-EFDA Contributors

# Design Study for ITER High Resolution X-ray Spectroscopy Array

# Design study for ITER high resolution x-ray spectroscopy array

R Barnsley[1], M.O'Mullane[2], L.C. Ingesson[3], A. Malaquias[4]
and JET-EFDA Contributors*

*Euratom/UKAEA Fusion Assoc., Culham Science Centre, Abingdon, OX14 3DB, UK.*
*[1]Department of Pure and Applied Physics, Queens University, Belfast, BT7 1NN, U.K.*
*[2]Department of Physics and Applied Physics, University of Strathclyde, Glasgow, G4 0NG, UK.*
*[3]EFDA Close Support Unit – Garching, Boltzmannstr. 2, D-85748 Garching, Germany.*
*[4]Associação Euratom/IST, CFN, Av. Rovisco Pais, 1049-001 Lisboa, Portugal.*

Preprint of Paper to be submitted for publication in Proceedings of the
15th HTPD Conference,
(San Diego California, USA 18-22 April 2004)

## ABSTRACT

The impurity line and continuum emission for ITER reference H-mode and ITB were modelled using the SANCO impurity transport code. Using the instrument sensitivity for a spatially resolving crystal spectrometer array with doubly-curved crystals and 2-D detectors, signals and signal-tonoise ratios were calculated for impurities including argon iron and krypton. These were shown to have lines suitable for the measurement of the ion temperature (0.5-30keV) and the rotation over almost the entire plasma minor radius. The main contribution to the signal-to-noise is the plasma continuum radiation on which the lines are superimposed. The main limitation to allowed impurity concentration is not the contribution to $Z_{eff}$, but the impurity radiated power, there being a broad operating range between about 100kW and 10MW. The spectrometer array has now been integrated into the ITER design.


## 1. INTRODUCTION

There is widespread effort to demonstrate space-resolving high-resolution x-ray spectrometers using doubly-curved crystals and 2-d detectors, for measurements of ion temperature and plasma rotation [1] [2] [3] [4] [5] . Based on predicted ITER Te and ne profiles, we have used the SANCO impurity ionization-transport code to model argon, iron and krypton radiated power, ion line-emission, and continuum emission at the relevant wavelengths. Using the calculated instrument sensitivity for a spatially resolving crystal spectrometer array, we simulate detector signals and signal-to-noise ratios, including n-$\gamma$ background.

A quasi-tomographic technique to reconstruct the Ti and rotation profiles, applied to various viewing options that separate the toroidal and poloidal rotation components, is reported by Ingesson et al in these proceedings[6].

## 2. EMISSION MODELLING

Figure 1 shows radial profiles[7] of Ti, Te and ne used for SANCO modelling of ITER H-mode and ITB plasmas. All the results for H-mode and ITB plasmas are similar, and only the H-mode data are presented here. The main constraint on the allowable added impurity concentration is not the increase in $Z_{eff}$, which is very small, but the additional radiated power, $\Delta P_{rad}$. The incremental radiated powers for added impurity concentrations of $10^{-5}$ .ne are: for Ar 0.25MW, for Fe 0.8MW and for Kr 1.4 MW. The radial profiles of $\Delta P_{rad}$ are strongly weighted towards the outer plasma (figure 2), and while the added impurity is inefficient to the extent that most of the $\Delta P_{rad}$ is not in the observed lines, radiative losses from the core are very low.

There is considerable overlap in the suitability of the various emission profiles (figure 3), but generally, $Kr34^{+}$, $Kr35^{+}$ and $Fe25^{+}$, with broad emission profiles peaked towards the core, are best suited for core measurements. Broad, slightly hollow emission profiles that are problematic for a single-chord system pose no problem, and are indeed are advantageous, for a continuously spaceresolved system. Better suited for the outer plasma, with hollow profiles and strong edge emission, are $Fe24^{+}$ , $Ar16^{+}$ and $Ar17^{+}$.

The free-free and free-bound continuum emission must also be modelled (figure 4), as it is relatively much stronger on ITER than existing tokamaks and, for a well-shielded detector, is the major source of noise on the Ti and rotation measurements. This is particularly true for Krypton, where the radiated power is shared over more ionization stages, and for a given $\Delta P_{rad}$ the line/continuum ratio is lowest.

If a consistent source of trace Fe can be achieved, then the observation of H-like Fe $25^{+}$, which has a very similar emission profile to $Kr34^{+}$, has several advantages. It requires a lower concentration and $\Delta P_{rad}$ for a given photon emission in the relevant spectral line, and the instrument sensitivity is much higher. Also, the H-like spectrum is not complicated by blends of satellite lines from lower ionisation stages, thereby simplifying reconstruction of radial profiles. A further advantage of Fe over similar-Z metals such as Ni, is that the relevant Fe wavelengths are very close to double those of Kr, making it possible to design a system that can observe both impurities with minimal adjustments.

## 3. DESIGN INTEGRATION

The present design has evolved form the ITER-98 design[8] [9]. Due to the long, narrow equatorial port plugs on ITER-98, a wide direct view of the plasma was impossible, and all poloidal spatial views except the central chord were achieved with graphite reflectors. In the present design, multiple imaging crystal spectrometers are located in upper and equatorial ports (figures 5 & 6). The shorter equatorial port of ITER-FEAT, and the upper port, together allow direct views of most of the plasma minor radius. The region $\sim 0.7 < r/a < \sim 0.9$ is inaccessible directly, and is viewed by two or more graphite reflectors, shown here in an upper port, though equally feasible in an equatorial port. Graphite has typical peak reflectivity of 30% and a band-pass of ~1%, with a further disadvantage that the reflection angles built into the port-plug must be carefully selected for specific wavelengths. The alternative of locating the spectrometers inside the port plug has been avoided on grounds of reduced access and increased background.

Various options for toroidal view and detector location have been designed. Figure 5 shows the maximum practical equatorial toroidal view of 18.5°. A spherical crystal requires a Bragg angle of ~50° (“A” in figure 5) which, within the space behind the port-plug, implies a crystal-detector distance of 1.5m, crystal radius of 2m, and port-detector distance less than 0.5m. The virtual entrance slit is about half-way down the port-plug. A toroidal crystal at ~30° Bragg angle (“B” in figure 5), may have poorer off-axis imaging, but otherwise has several advantages. The portdetector distance of 2.3m facilitates detector shielding and access, while detector-crystal distance of 2.5m implies a primary crystal radius of 5.3m, and improves input shielding by placing the virtual entrance slit closer to the blanket penetration. For both options, an asymmetric crystal cut could place the virtual slit much closer to the blanket penetration. Both options require a conical slot in the port-plug for optimum input shielding, this effect being less for option “B”. The reduced angular dispersion of “B” is balanced by its longer detector arm, so that the required detector resolution for $\lambda/\delta\lambda$ = 10 000 is about 0.25mm in both cases.

The total required detector height of ~800mm is determined by the demagnification of ~0.2, and is independent of the number of crystals used to cover the total viewing angle. About five individual detectors are required, with height of 150-200mm in the imaging direction, with a spatial resolution of ~5mm, allowing >100 resolvable chords. In the $\lambda$-direction, a width of ~50mm with resolution of 0.1-0.25mm is required. The peak count-rate density is ~$10^7$ count/$cm^2$ .s with an average of $10^6$ count/$cm^2$ .s. For signal-to-noise estimates, we have assumed a n-g background count density of $10^5$ count/$cm^2$ .s, based on an unshielded flux of $10^7$ n-$\gamma$/$cm^2$ .s and an attenuation factor of 100, due to a shield transmission of 10% and detector sensitivity of 10%. This is conservative estimate compared to JET where, as discussed below, a background attenuation of $10^6$ was achieved. The required performance is typical of detectors in use or in development for high-flux sources. These include gas-microstructure proportional counters and solid state arrays with individual pulse processing chain for each pixel.

## 4. SENSITIVITY

The count-rate $N'_\lambda$ (count/s) from a spectral line with intensity $I_\lambda$ (photon/$cm^2$.s), is given by:

$$N'_\lambda = I_\lambda \cdot S_\lambda$$

For a Johann spectrometer with graphite prereflector, the sensitivity function $S_\lambda$ ($cm^2$) is:

$$S_\lambda = Pgr_\lambda \cdot \frac{\kappa \cdot \psi \cdot Rc_\lambda}{4 \cdot \pi} \cdot hx \cdot hy \cdot \eta_\lambda$$

with graphite peak reflectivity Pgr, crystal filling-factor $\kappa$ ($\kappa$=1 with suitable input geometry), vertical divergence $\psi$ (rad), crystal reflection integral Rc (rad), crystal projected area hx.hy, and combined window/detector efficiency $\eta$. For a total vertical divergence $\psi_{tot}$, and for $n_{ch}$ viewing channels, the vertical divergence per channel is$\psi ch = \psi_{ot} / n_{ch}$.

Sensitivities for a Fe/Kr 1st /2nd order Graphite(002/004)-Ge(220/440) system (table 1) were used for all the signal estimates here, and by Ingesson et al for the accompanying reconstruction analysis. Higher Kr sensitivity can be achieved in 1st order, but the shallow Bragg angles would be a challenge for imaging optics. Sensitivities for spherical crystals at Bragg angles close to 50°, would be similar to those used here, and would not significantly change the results.

## 5. BACKGROUND RADIATION

Neutron scattering has been modelled[10] for the upper port system, where figure 7 shows the direct flux at the crystal, and the scattered flux at the detector location assuming no additional shielding behind the port-plug. There are two sources of detector background; firstly scattering along the optical path into the detector of the direct flux incident on the crystal, and secondly the general background at the detector due to secondary scattering, incomplete shielding by the port-plug, and other port penetrations. Background measurements during D-T experiments on

JET have enabled these two noise sources to be quantified and largely isolated from each other.

The JET double-crystal spatially scanning spectrometer[11] was inside the torus hall, mounted to an upper port, with its 12mm deep Ar-filled detector shielded by 0.1m of Pb surrounded by 1m of borated polyethylene. The two-reflection optics prevented a direct line of sight from the detector to either the plasma or the first crystal, so that transmission through the shield was the main source of detector background. In the JET preliminary tritium experiment (PTE-1991), background in the detector was 100 count/cm$^2$.s, for an estimated neutron flux of $10^8$ n/cm$^2$.s outside the detector shield, representing an effective attenuation factor of $10^6$.

The JET Bragg survey spectrometer[12] , located on an 18m vacuum beam-line[13] outside the JET 3m concrete bio-shield, has its 4mm deep, Ar-filled low-energy detector only 50mm from the plasma-facing crystal. In the JET D-T experiment of 1997, the background in this detector was 1000 count/cm$^2$.s for a direct neutron flux at the crystal of $10^9$ n/cm$^2$.s. Some fraction of that background was due to secondary scattering within the spectrometer bunker, so the effective attenuation factor of $10^6$ represents a lower limit.

Together, these results show that the background count-rate due to scattering of direct n-$\gamma$ flux from crystal into detector is very low, and that a gas-filled detector can be well shielded from indirect background radiation at levels predicted behind an ITER port-plug. Similar results for VUV/XUV spectrometers with micro-channel-plate detectors are presented in these proceedings by Coffey[14].

## 6. SIMULATED SIGNALS

Figure 8 shows the simulated count-rate per chord, for 35 chords, for the principal emission lines of H- and He-like ions of Ar, Fe and Kr, namely 1s-2p Ly$\alpha_1$, and the 1s$^2$ -1s2p “w” line.

Given the lower radiation efficiency and lower spectrometer sensitivity for He-like Kr compared to H-like Fe, the $\Delta P_{rad}$ required for a given count-rate, and hence signal-to-noise ratio, is much higher for Kr. Expressed in terms of $\Delta P_{rad}$/count-rate, the central-chord values are typically: for Ar 250MHz/MW, for Fe 40MHz/MW, and for Kr 1MHz/MW. Most preceding ITER design studies have been based on Kr, but these results suggest that for the smaller plasma of ITER-FEAT, the main reason to use Kr is for its easier introduction into the plasma, not its ionization balance, and that any of the metals in the Fe-Zn range would be preferable for core measurements if a consistent source could be achieved.

## CONCLUSION

Based on emission modelling of suitable lines of Ar, Fe and Kr, a space-resolving high-resolution crystal spectrometer array for Doppler Ti and rotation measurements over the full plasma r/a has been integrated into the ITER design. The main limitation to allowable impurity concentration is not the contribution to $Z_{eff}$, but the impurity radiated power, there being a broad operating range between about 100kW and 10MW. Detector background measurements from JET D-T experiments, in conjunction neutron modelling for the ITER design, show that shielding and background noise will be adequate for ITER. Good signal-to-noise ratios can be achieved with 100ms integration time, for impurity radiated power less than 500kW, the main contribution to the signal-to-noise being the plasma continuum radiation on which the lines are superimposed. An accompanying study[6] of the optimization of sight-lines and profile reconstruction for the various spectral lines, shows that good radial coverage can be achieved with $Fe25^{+}$ for the core and $Ar17^{+}$ for the outer plasma, with considerable overlap.

**ACKNOWLEDGMENTS**

This work was carried out under a contract from the European Fusion Development Agreement and funded by the UK Engineering and Physical Sciences Research Council and EURATOM.

**REFERENCES**

[1]. M Bitter, Spatially Resolved Spectra from an X-ray Imaging Crystal Spectrometer. These proceedings

[2]. S G Lee, Research and development of X-ray imaging crystal spectroemters for KSTAR. Ibid.

[3]. G Bertschinger Compact imaging Bragg spectrometer for fusion devices. Ibid.

[4]. M Nelson, High resolution soft X-ray spectrometer on the MAST tokamak. Ibid.

[5]. K W Hill, First experimental results from a high resolution Bragg imaging spectrometer on NSTX and Alctor C-MOD. Ibid.

[6]. C Ingesson, Optimization of the lines of sight of the Iter X-ray crystal spectrometer diagnostic. Ibid.

[7]. A Loarte, EFDA-CSU, Garching, Germany.

[8]. R Barnsley et al In "Diagnostics for experimental thermonuclear fusion reactors 2", Ed. Stott et al. Plenum Press, New York (1998) p**307**.

[9]. P H Edmonds et al. Ibid. p**79**

[10]. Dr Lida, ITER-IT, Garching, Germany.

[11]. U Schumacher et al, Continuously space-resolved X-ray spectroscopy at JET. Rev. Sci. Instrum. vol.60 no.4 April 1989 pp.**562-566**.

[12]. R Barnsley et al, Bragg rotor spectrometer for tokamak diagnostics, Rev Sci Instrum. **57**(8)Aug.1986 (2159)

[13]. R Barnsley et al, JET Beamline with Integrated X-ray, VUV, and Visible Spectrometers, for Burning Plasma Experiments. Rev Sci Instrum, April 2003.

[14]. I Coffey, First tritium operation of ITER-prototype VUV spectroacopy on JET. These proceedings.

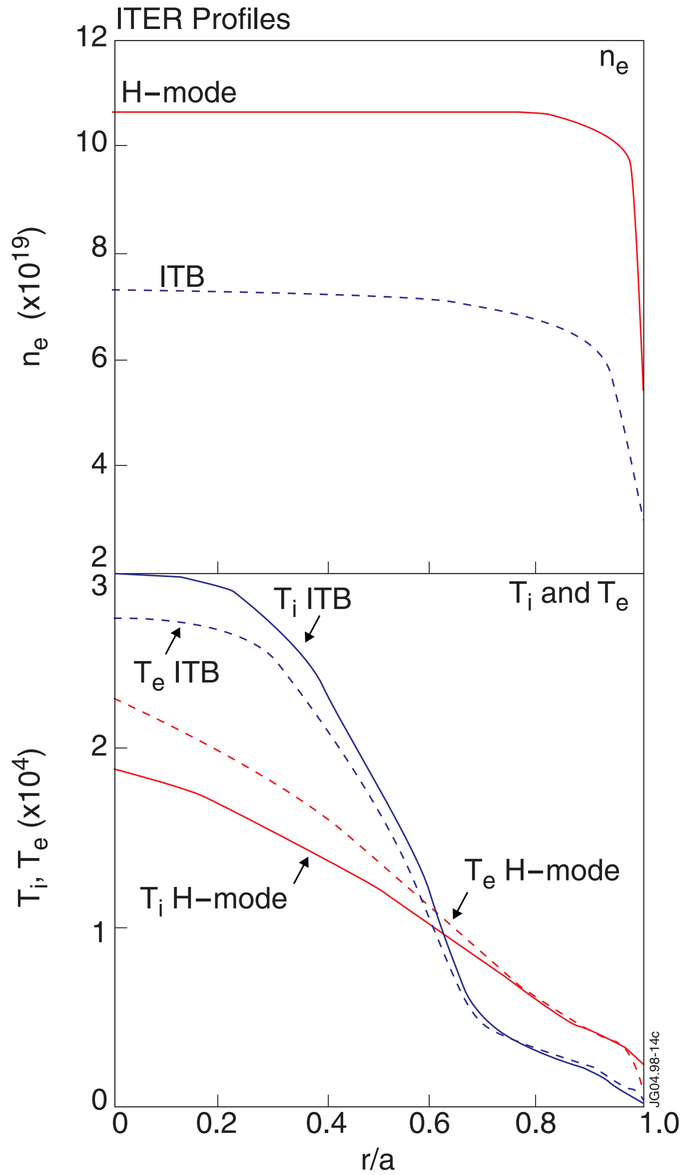


*Fig.1. Radial profiles of ne, Te, and Ti for ITER H-mode and ITB plasmas, used for SANCO and signal simulations.*

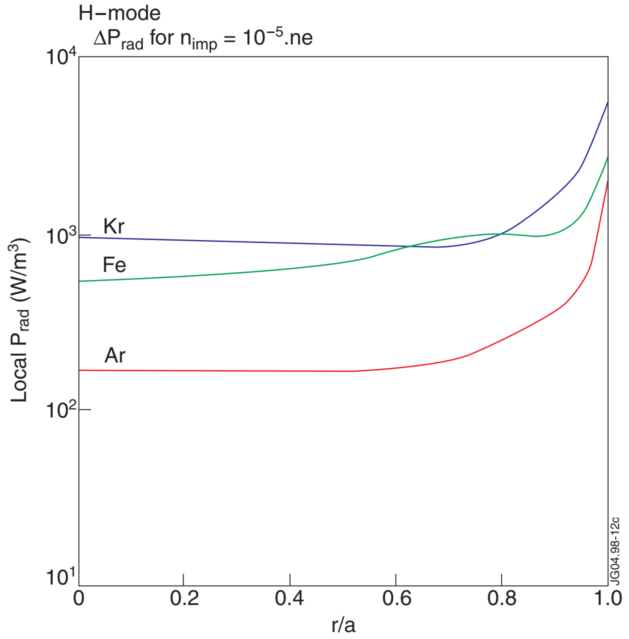


*Fig.2. H-mode radial profiles of local $\Delta P_{rad}$ for Ar, Kr & Xe at nimp/ne = $10^{-5}$*

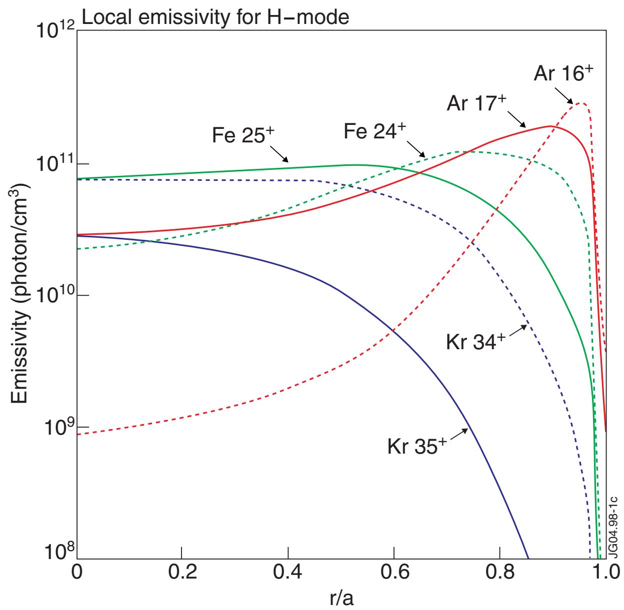


*Fig.3. Local emissivity for H- and He-like Ar, Fe and Kr ions at $\Delta P_{rad}$ = 500kW in each case. There is good emission over the whole plasma, suitable for Ti and rotation measurements.*

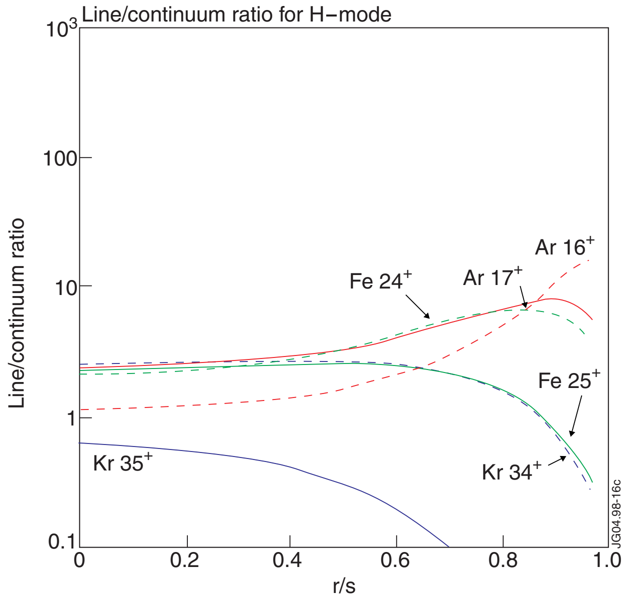


*Fig.4. Line/continuum ratios*

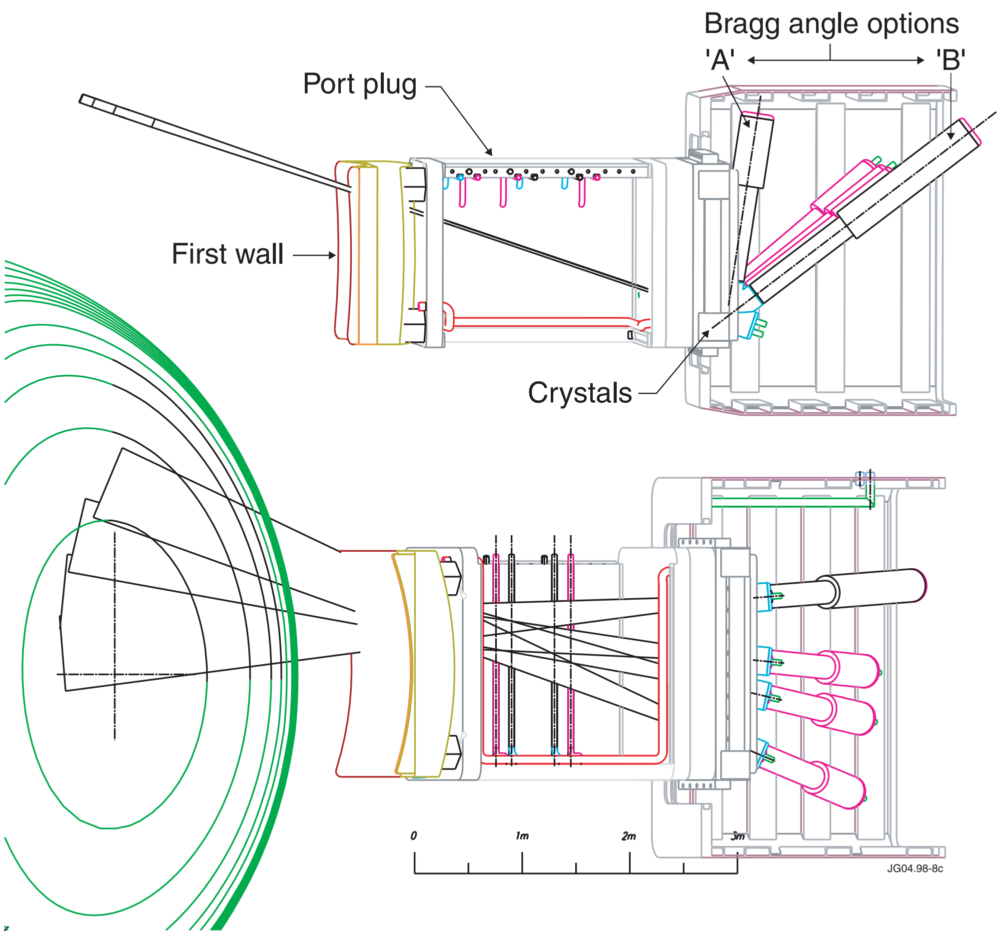


*Fig.5. Schematic of the equatorial port array of imaging spectromet*

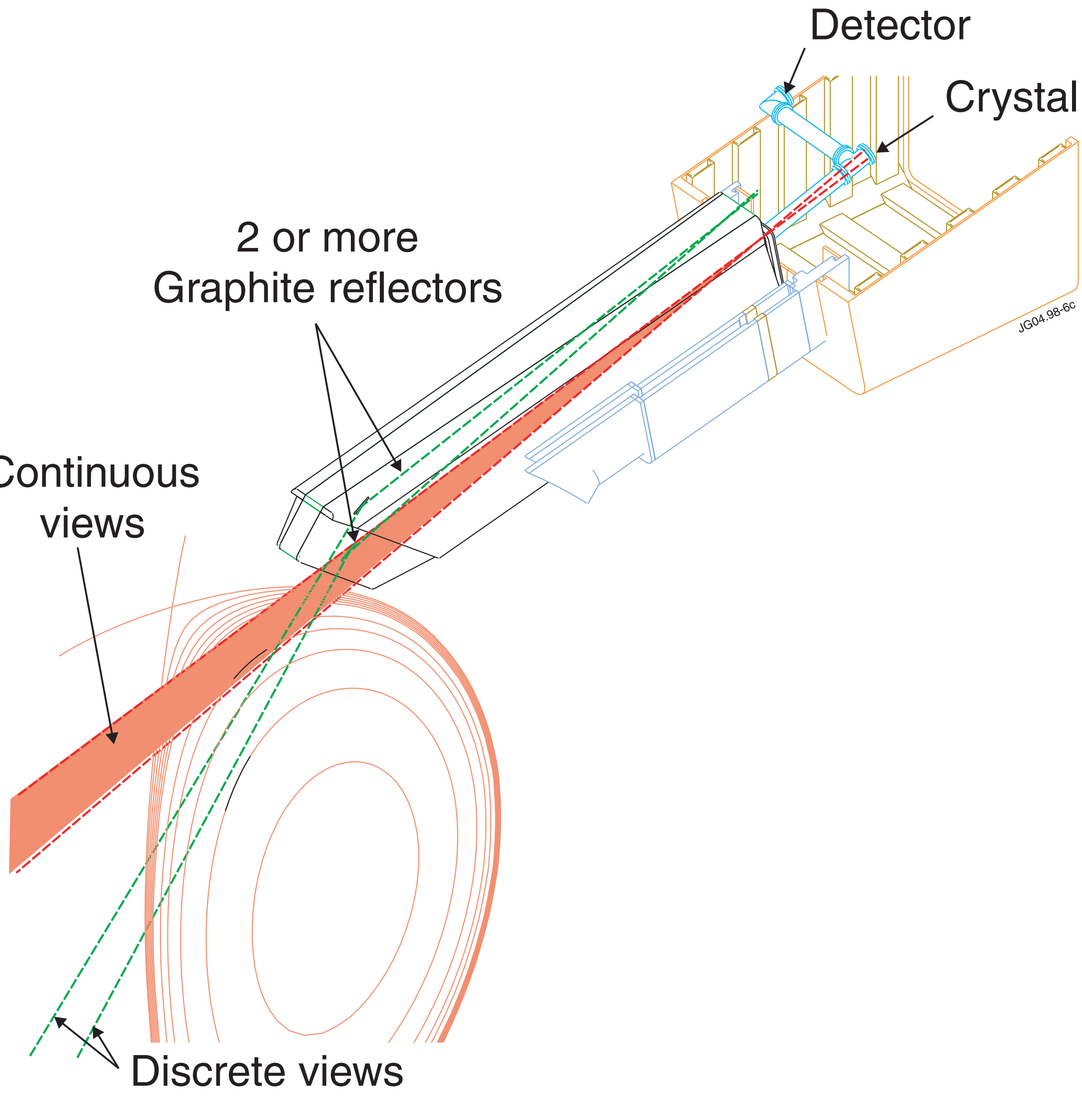


*Fig.6. Schematic of the imaging x-ray crystal spectrometer, and discrete-chord graphite reflectors, in an upper port.*

| | **Reference Fe in 1$^{st}$ order** He-like Fe 24$^{+}$ 1s$^{2}$-1s2p 0.185 nm | **Reference Kr in 2$^{nd}$ order** He-like Kr 34$^{+}$ 1s$^{2}$-1s2p 0.0946 nm | High sensitivity Kr in 1st order |
|---|---|---|---|
| Graphite planes | (002) | (004) | (002) |
| Graphite $\theta_B$ | 16.0° | 16.4° | 8.1° |
| Graphite peak Reflectivity $P_{gr}$ | 0.3 | 0.2 | 0.5 |
| Germanium planes | (220) | (440) | (220) |
| Germanium $\theta_B$ | 27.55° | 28.23° | 13.68° |
| Ge reflection integral $R_c$ (μrad) | 66 | 9 | 34 |
| **$S_D$ Direct views** ($10^{-7}$ cm$^2$) | 9.4 | 1.3 | 4.7 |
| **$S_{Gr}$ Graphite views** ($10^{-7}$ cm$^2$) | 2.8 | 0.25 | 2.4 |

JG04.98-15c

*Table 1. Calculated instrument sensitivities per channel for 35 channels, $\psi_{tot}$ ~ 0.5 rad, $n_{ch}$ = 35, crystal aperture $h_x \cdot h_y$ = 5 x 5cm$^2$, and a combined window/detector efficiency $\eta$ = 0.5.*

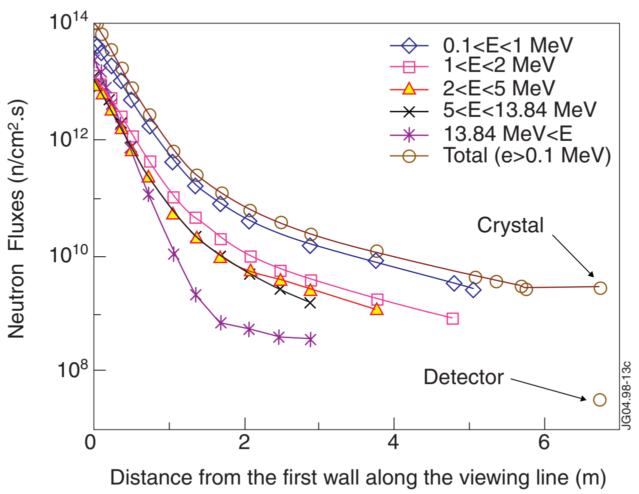


*Fig.7. Modelled neutron levels for the ITER upper port system.*

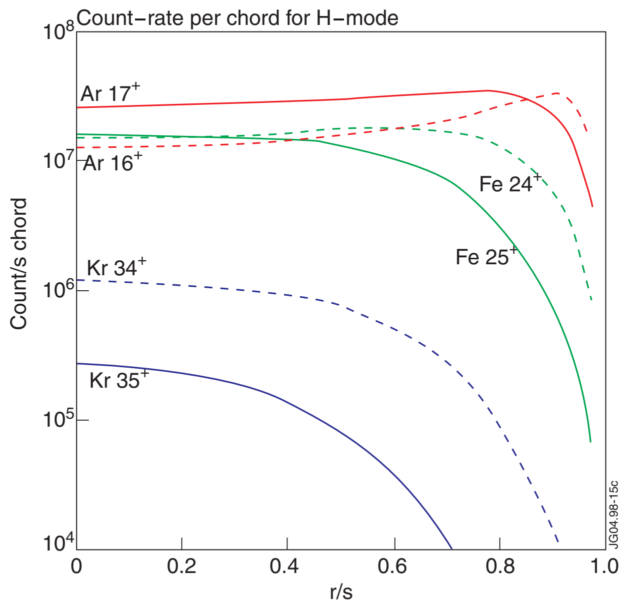


*Fig.8. Detector count-rate per chord for 35 channels*